Predicting Biological Gender and Intelligence from fMRI via Dynamic Functional Connectivity

Bhaskar Sen, *Student Member, IEEE*, and Keshab K. Parhi, *Fellow, IEEE*

***Abstract*— Objective: This paper explores the predictive capability of *dynamic* functional connectivity extracted from functional magnetic resonance imaging (fMRI) of the human brain, in contrast to static connectivity used in past research. *Methods:* Several state-of-the-art features extracted from *static* functional connectivity of the brain are employed to predict biological gender and intelligence using publicly available Human Connectome Project (HCP) database. Next, a *novel* tensor parallel factor (PARAFAC) decomposition model is proposed to decompose sequence of *dynamic* connectivity matrices into common connectivity components that are orthonormal to each other, common time-courses, and corresponding distinct subject-wise weights. The subject-wise loading of the components are employed to predict biological gender and intelligence using a random forest classifier (respectively, regressor) using 5-fold cross-validation. *Results:* The results demonstrate that *dynamic* functional connectivity can indeed classify biological gender with a high accuracy (0.94, where male identification accuracy was 0.87 and female identification accuracy was 0.97). It can also predict intelligence with less normalized mean square error (0.139 for fluid intelligence and 0.031 for fluid ability metrics) compared with other functional connectivity measures (the nearest mean square error were 0.147 and 0.037 for fluid intelligence and fluid ability metrics, respectively, using *static* connectivity approaches). *Conclusion:* Our work is an important milestone for the understanding of non-stationary behavior of hemodynamic blood-oxygen level dependent (BOLD) signal in brain and how they are associated with biological gender and intelligence. *Significance:* The paper demonstrates that *dynamic* behavior of brain can contribute substantially towards forming a fingerprint of biological gender and intelligence.**

***Index Terms*— fMRI, Prediction of gender, Intelligence Prediction, Tensor Decomposition, resting-state, task, functional connectivity, dynamic, Human Connectome Project, PARAFAC.**

I. Introduction

This paper presents classification and regression approaches to predict gender and intelligence of humans from the functional magnetic resonance imaging (fMRI) of the brain. In particular, the paper investigates the predictive power of *dynamic* functional connectivity (dFC) for classifying biological gender and intelligence metrics. The results are compared with *static* connectivity and it is shown that dFC is predictive of two important phenotypes in humans. We use a large dataset containing task and resting state fMRI data of 475 subjects (each subject performed 7 tasks, *e.g.*, *emotion, gambling, working memory, relational, social, motor, language* as well as rest) from the Human Connectome Database [1] to test the classification method.

Dynamic functional connectivity of human brain refers to change in spatio-temporal organization of neuronal units over time [2], [3]. *Dynamic* connectivity was known previously to exist for brain scanning modalities with rich temporal resolution, *i.e.*, electroencephalography (EEG), magnetoencephalography (MEG) [4]–[8]. However, only recently dFC was shown to be present in functional magnetic resonance imaging (fMRI) [9]. Since then, several papers have investigated how dFC correlates with demographic characterization (e.g., age [10], gender [11], intelligence [12] and cognition [13]). *Dynamic* functional connectivity has also been demonstrated to be associated with disease states [14]–[16]. There has been an interest in using dFC for individual characterization specifically for prediction studies – dFC was used in [17], [18] for classifying gender [17], psychiatric disorders [19] and for predicting attention load [20].

Given the plethora of work with evidence that dFC is an important phenomena in *neuroimaging*, our understanding is still constrained about the possible personal characteristics that can be predicted based on dFC. This paper shows that dFC can contribute substantially towards forming a *fingerprint* for classifying biological gender and predicting intelligence quotient (IQ) based on behavioral tasks. Predicting IQ from dFC has not been reported in literature before, and is a major contribution of our work. Additionally, it is shown that dFC can match, or sometimes outperform, other standard MRI-based models for classification of biological gender [17]. This paper presents a novel way to extract dFC *states* from task fMRI (t-fMRI) and resting state fMRI (rs-fMRI). The *states* are formulated as a constrained tensor decomposition problem that has a unique solution. An algorithm utilizing alternating least square technique is derived that identifies the unique component *states*.

The paper considers the analysis of both task-fMRI (t-fMRI) and resting-state fMRI (rs-fMRI). A brief description of t-fMRI or rs-fMRI is given next. During t-fMRI, the person performs a number of repetitive tasks, *e.g.*, tapping fingers, watch pictures, make decision etc. while inside the scanner. These behaviors invoke the hemodynamic response known as

Manuscript received April 19, 2020; revised July 1, 2020; accepted July 18, 2020. This research was supported in part by the National Science Foundation by grant number CCF-1954749.

Bhaskar Sen and Keshab K. Parhi are with Department of Electrical and Computer Engineering, University of Minnesota, Minneapolis (e-mail: parhi@umn.edu)

blood-oxygen level dependent (BOLD) signal corresponding to the repetitive task [21]. Task fMRI contain valuable information about a subject's behavioral abilities, gender [22], and age [23]. On the other hand, rs-fMRI measures the spontaneous fluctuation of BOLD signal during awake rest. In case of many psychiatric illnesses, rs-fMRI signal of the patient is highly meaningful and predictive of individual traits [24] and psychiatric disorder [25]–[27].

A. Prior Work

1) Gender effect on dFC is not well characterized: In recent years, a number of studies have found brain functional connectivity differences for different biological gender using various neuroimaging modalities. These differences are especially prominent in several cognitive and behavioral characteristics, such as verbal abilities, working memory abilities and spatial orientations [28]. However, these studies have mainly addressed the psychometric or behavioral differences at the group population level. Whether functional connectivity differences have predictive capability of biological gender is of utmost interest. A few prior publications have also investigated functional and anatomical brain network dissimilarities for classifying male $vs.$ female [29]–[31]. Anatomical connectivity differences for biological gender were reported in [29] using structural diffusion tensor imaging (DTI). Zhang et al. [30] used rs-fMRI and partial least square modeling to classify gender. Moreover, global network properties extracted from *static* connectivity were found to differ in emotion regulation [31]. Stronger functional connectivity has been noticed in default mode network for females. Particularly, Buhm et al. [32] concluded that functional networks consisting of posterior cingulate cortex (PCC), precuneus and bilateral medial prefrontal cortex are active for females in rs-fMRI. Strong intra-hemispheric network connectivity were reported in females whereas strong inter-hemispheric connections were prominent for males [33] during rest. Similar conclusion was also reached in the case of anatomical networks [34]. Although predicting biological gender based on *static* functional connectivity and anatomical connectivity are well studied, there is lack of scientific literature on understanding the predictive ability of *dynamic* connectivity for biological gender. Recent work by [17], [18] have made preliminary progress in this direction. Menon et al. [17] were successful in classifying biological gender based on intrinsic functional connectivity such as edge consistency, edge variability and differential power measures. The partial *static* connectivity and dFC were able to classify biological gender with an accuracy of 0.90 and 0.80, respectively, in a leave-one-out model. Default Mode Network and visuospatial networks were found to have moderate variability among groups. Additionally, fronto-parietal and attention networks had high functional variability. Cai et al. [18] performed an association study using rs-fMRI data to investigate biological gender differences. This study employed a novel GICA-TVGL framework and observed that males and females have significant differences with respect to visual network. Additionally, differences in dFC state transition time was reported.

2) IQ affect on dFC is not well characterized: Similarly, the predictability of IQ from dFC is not well characterized. A few studies have attempted to associate and predict individual intelligence metrics from structural and functional MRI until now. Among them, the work by Finn et al. [35] was able to successfully establish the importance of *static* connectivity to predict fluid intelligence using a cross-validation and machine-learning modeling. Additionally, Dubois et al. [36] conducted a study by utilizing a fully cross-validated model to show that functional connectivity in human brain could predict 20 percent of the total variations for the intelligence distribution in population. The model was built by the factor analysis of intelligence scores for 10 different tasks. Similar study was carried out in [37] and it was concluded that functional activation maps of brain is predictive of general intelligence. Although progress has been made to associate intelligence with functional connectivity profile of brain, very few studies have demonstrated the predictability of intelligence quotient (IQ) using non-stationary functional profile of brain activity. In addition, more work needs to be done to understand whether finding from one cohort of subjects can directly be extrapolated to different sub-groups of populations.

3) Computing Dynamic Functional Connectivity: The most common way of extracting dFC from fMRI is by sliding-window correlation matrix. Since fMRI is spatio-temporal, one can conceive of the network of the spatial pattern to be *dynamic* instead of *static*. A very interesting direction in fMRI neuroimaging study is the extraction of spatial couplings that vary over time. In order to extract the spatial couplings, blind source separation (BSS) models, in particular, independent component analysis (ICA), non-negative matrix factorization, principal component analysis and tensor decomposition, have been widely adapted in data-driven pattern studies [38]–[41]. A study by Kiviniemi et al. [40] investigated the stability of ICA components over time segments to understand the changes in spatial coupling of the default mode network. In another model, an atlas is used to parcellate the brain into spatial maps using BSS, where each map has distinct time courses associated with it. Following this, the time-varying property of the component time courses [42] is captured by calculating Pearson's correlation using windowing [43], [44]. Following this, ICA, PCA, etc. are performed to find out the brain states. Although PCA and ICA are widely used for extracting *dynamic* functional connectivity, they suffer from two drawbacks. PCA decomposition constrains both connectivity maps as well as the time courses (activity level) of the maps to be orthogonal to other maps and time courses. This can severely hamper the expressiveness of model. ICA can overcome the orthogonality constraint in the time domain, although the uniqueness of spatial maps requires the sources to be non-Gaussian. Tensor decomposition, specifically PARAFAC decomposition, can alleviate both concerns, as the required constraints can be added to a particular mode without affecting other modes.

B. Contribution

The contribution of this paper is four-fold.

- The paper presents *yet* another method for extracting dFC from sliding window correlation using tensor decomposition. The uniqueness conditions for the tensor decomposition are formulated. In addition, we provide an algorithm utilizing alternating least square based approaches for finding the unique decomposition.
- The paper investigates the importance of dFC for biological gender classification from fMRI. It is shown that gender can be predicted accurately from most of the task-related connectivity patterns in brain.
- The paper successfully demonstrates the importance of dFC for prediction of intelligence metrics from fMRI. We find that subject-wise weights of *dynamic* spatio-temporal maps are predictive of intelligence.
- The paper proposes a novel method to extract related *dynamic* sub-networks associated with gender and intelligence prediction. Statistical tests are also carried out to validate the significance of the proposed sub-networks.

II. PARAFAC-BASED DECOMPOSITION MODEL

A. Notations

In this paper, tensors are denoted in caligraphic letters (*e.g.*, $\mathcal{X}$), matrices in uppercase letters (*e.g.*, A) and vectors in lowercase letters (*e.g.*, a_f). $||.||_F$ denotes Frobenius norm, $\odot$ denotes Khatri-Rao product, $*$ denotes Hadamard product.

B. Preliminaries

Regional time-series from each fMRI scan are extracted and they are reshaped to a matrix ($\dim\ 1 =$ spatial, $\dim 2 =$ temporal. From this matrix, a new *dynamic* connectivity matrix based on sliding window of pre-defined strides are formed. More details can be found in Section III (Experimental Setup). In brief, each subject's regional time-series yield multiple time-series windows based on their strides, which are then used to create Pearson's correlation between regions for each time-window. Following this, the Pearson's correlation matrices are vectorized and multiple connectivity vectors are stacked to create a dFC matrix for each subject where ($\dim 1 =$ edges, $\dim 2 =$ temporal). The scans from a group of subjects are concatenated to form a 3-way tensor where the $\dim 3 =$ subject. We denote the 3-way tensor of size $I_1 \times I_2 \times I_3$ as $\mathcal{X}_{I_1,I_2,I_3}$.

C. Traditional PARAFAC

Traditional unconstrained PARAFAC [45] modeling for decomposing a tensor $\mathcal{X}_{I_1,I_2,I_3}$ into F number of rank-1 tensors can be written as

$$\mathcal{X}_{I_1,I_2,I_3} = \sum_{f=1}^{F} a_f \circ b_f \circ c_f,\ \mathcal{X} = (A,B,C) \quad (1)$$

where A, B, C are of size $I_1 \times F$, $I_2 \times F$ and $I_3 \times F$ respectively. $a_f = A_{:,f}$, $b_f = B_{:,f}$, $c_f = C_{:,f}$ where $A_{:,f}$ is the f^{th} column of A and $\circ$ denotes outer product. For unconstrained PARAFAC decomposition, each rank-1 tensor will consist of one matrix (A) representing spatial couplings (column in A), corresponding time variation of the component (each column of B) and the distinct weights of the time-varying spatial-coupling map for each subject (column in C). Precisely, this decomposition optimizes the following function:

$$\min_{A,B,C} ||X_1 - (C \odot B)A^T||_F^2 \quad (2)$$

where $X_1 = X_{I_2 I_3, I_1}$. More specifically, X_1 is tensor $\mathcal{X}$ reshaped as a matrix with number of rows $I_2 \times I_3$ and columns I_1. Likewise we also define $X_2 = X_{I_3 I_1, I_2}$ and $X_3 = X_{I_2 I_1, I_3}$ where X_2 and X_3 correspond to reshaped matrix form of tensor $\mathcal{X}$. Previous works have shown that unconstrained PARAFAC decomposition itself is unique under very mild conditions [45]–[47].

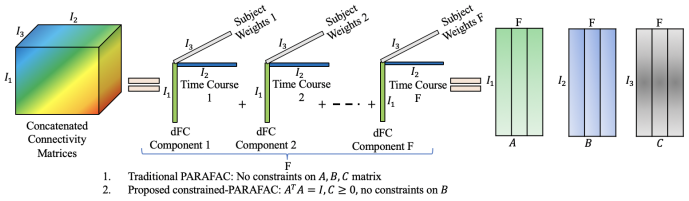

Fig. 1: PARAFAC decomposition conceptual illustration. A 3-D tensor is divided into rank-1 tensors where each of them is outer product of three vectors. The outer product vectors for each dimension from rank-1 tensors are collected in matrices.

D. Constrained-PARAFAC

Although unconstrained PARAFAC tensor may have unique decomposition under mild conditions, the optimization process used to find the decomposition matrices may introduce many correlated components [45]. Moreover, in the case of decomposing *dynamic* connectivity tensor into common spatio-temporal components, it may introduce connectivity profiles that are hard to interpret from a biological perspective. Thus in order to alleviate these two problems, we introduce orthogonality in $\dim -1$. This guarantees that the spatial connectivity components extracted from the tensor are uncorrelated. In addition, we ensure that the decomposition profile is validated by previous work on BSS for fMRI (using ICA, PCA) which follows the hypothesis that cross-talk among spatial-coupling should be small [19], [48]. These two cases are satisfied by using $A^TA = I$, where I is a identity matrix. Also, for interpretability, we can assume the weighting of spatio-temporal maps in each subject to be non-negative ($C \geq 0$). Thus, decomposition problem has milder uniqueness conditions than traditional PARAFAC. The corresponding uniqueness and an efficient algorithm for finding these components are derived later. A conceptual illustration of PARAFAC and the proposed constrained-PARAFAC models is shown in Fig. 1.

The corresponding optimization is stated as:

$$\min_{\tilde{\mathcal{X}}} ||\mathcal{X} - \tilde{\mathcal{X}}||_F^2\ s.t.\ \tilde{\mathcal{X}} = (A,B,C), A^TA = I,\ C \geq 0 \quad (3)$$

Note that each sub-problem (for A, B and C) can be solved optimally using generalized solution to the orthogonal procrustes problem [49], generalized least square solution [50] and non-negative least squares solution [51], respectively.

This constrained-PARAFAC decomposition was proposed in [21] for extracting the *static* functional activation maps from

raw fMRI data. In contrast, this paper utilizes the decomposition model for extracting *dynamic* spatial couplings that vary over time and uses the distinct subject-wise loading vectors to associate and predict gender (respectively, intelligence) from both t-fMRI and rs-fMRI. Here we note that, although the proposed tensor decomposition has straightforward interpretations for t-fMRI since all subjects perform pre-scheduled tasks, resting-state fMRI is not synchronized among subjects. However, during rest, fMRI scans have shown synchronization among regions of brain in humans. This is especially true for the default mode network (DMN) [25] in brain. Recently, *trilinear* tensor factorization was also applied explicitly to rs-fMRI in [8], [52], *i.e.*, time courses were synchronized among subjects. We explored the predictive performance of the same technique as an exploratory measure for rs-fMRI as well as to predict biological traits. The model performance showed that straightforward application of constrained-PARAFAC tensor decomposition is useful for rs-fMRI for classification of biological gender and prediction of intelligence.

1) Uniqueness: Uniqueness conditions for the proposed model are derived in the following two theorems.

Theorem 1. Consider $\mathcal{X} \in \mathcal{R}^{I_1 \times I_2 \times I_3}$. Let $A \in \mathcal{R}^{I_1 \times F}, B \in \mathcal{R}^{I_2 \times F}, C \in \mathcal{R}^{I_3 \times F}$ represent the tensor decomposition matrices such that $C \geq 0$ and $A^T A = I$. In this case a global minimum for (3) exists. In other words, there is only one solution for $\tilde{X}$ that minimizes (3).

Proof. The proof is given in Supplementary Information Section Proofs Subsection A.

Now we state the two conditions that need to be satisfied for the decomposition to be unique.

Condition I. B does not have proportional columns.

Condition II. C has full non-negative column rank.

Theorem 2. If conditions *I* and *II* are satisfied, then the decomposition $\tilde{X} = (A, B, C)$ is unique up to permutation and scaling.

Proof. The proof is given in Supplementary Information Section Proofs Subsection B.

2) Algorithm for Solving the Problem: An algorithm for finding the solution of (3) is given in Algorithm 1.

Theorem 3. Algorithm 1 finds the uniquely identifiable decomposition of (3).

Proof. The proof is given in Supplementary Information Section Proofs Subsection C.

Algorithm 1: Alternating Least Square Algorithm for Solving Constrained PARAFAC in (3)

Input : Tensor $\mathcal{X}$, rank F
Output: Estimated connectivity maps A, time courses B, subject-wise contribution C

(X_1, X_2, X_3) = Unfold $\mathcal{X}$ along axis 1, 2, 3 respectively.
Initialize A, B, C
for $i = 1$ **to** *until convergence* **do**
  % Solve for A from unfolding X_1
  $M = [(B \odot C)^T X_1]$
  $M = U \Sigma V^T$
  $A^T = U V^T$
  % Solve for B from unfolding X_2
  $B^T = [(C \odot A)^T X_2]$
  % Solve for C from unfolding X_3
  $N = (A \odot B)^T X_3$
  $C^T = [N_+]$
  where N_+ contains only the positive elements of N
end

III. Experimental Setup

A. Dataset

The dataset used in the analysis is taken from Q2 release of Human Connectome Project database [1], [53]. The dataset consisting of 475 subjects is used to classify gender (male vs. female) and predict intelligence of the subject. The subjects in the database were scanned while they performed the following seven tasks i) emotion, ii) gambling, iii) working memory, iv) relational, v) language, vi) motor, vii) social. Additionally rs-fMRI was also captured.

1) Biological Gender: Number of females 279, number of males 196.

TABLE I: Demographic and task score information for the subjects.

Demographic Information	Male	Female	Range
# of samples (n)	196	279	-
Age – mean (SD)	29.30 (3.31)	29.23 (3.48)	22-36
Task Score Information	Male	Female	Range
Fluid Intelligence - mean (SD)	16.56 (5.21)	15.76 (5.13)	4-24
Fluid Ability Metrics - mean (SD)	99.50 (16.35)	101.85 (16.14)	47-150

2) Intelligence: Following [1], two relevant behavioral tasks were chosen as metrics of intelligence [24] quotient. Table I provides the the age and task scores along with the range of score values. There were no significant differences ($p > 0.05$) between males and females with respect to the scores.

- *Fluid Intelligence*. Fluid intelligence was measured using the Penns Progressive Matrices (PMAT) [54]. PMAT is a shortened version of Ravens Progressive Matrices. In this test, the participants were given puzzles that contained visual patterns. In the puzzles, a piece was missing and they were asked to fill the blank piece from a number of candidate pieces.
- *Fluid Ability Metrics.* The Pattern Comparison Processing Test is a measure of speed of processing, which is considered a 'fluid ability' because it steadily improves from childhood to adolescence, and then begins to decline in adulthood (Range 47-150). This test for ages 7-85 asks participants to identify if the two pictures shown in the screen are same. The age-adjusted scale score was used for our experiment. Participant score was normalized using the age appropriate band of Toolbox Norming Sample (bands of ages 18-29, or 30-35). A score of 100 signifies performance that is same as national average, whereas a score one standard deviation away corresponds to an increase or decrease of 15 points.

B. Data Acquisition and Preprocessing

The fMRI dataset consisted of 475 subjects taken from Human Connectome Project database [1], [53]. All the tasks and

resting state data were used. The fMRI data can be publicly accessed from [1]. Functional magnetic resonance imaging data were acquired using a customized Siemens 3T Connectome Skyra scanner. The scans were taken using 2 mm isotropic voxels with TR = 720ms, TE = 33.1 ms as described in [55]. Details of the task paradigms can be found in WU-Minn HCP 500 Subjects Data Release Manual available from [2].

The HCP fMRI data was first processed following the HCP fMRI Volume pipeline (v3.4), which includes gradient unwrapping, motion/distortion correction, registration to structural scan, nonlinear registration into MNI152 space, and intensity normalization as reported in [56]. Subsequently, spatial smoothing and activation maps generation using the generalized linear model implemented in FSLs FILM (FMRIBs Improved Linear Model with autocorrelation) were performed. Using Freesurfer cortical parcellation atlas [57], 85 regions of interest were identified as shown in Table R1 in Supplementary Information. Mean time-series values of voxels in every region for each subject were then extracted. For *static* connectivity analysis, one-shot absolute Pearson's correlation values are extracted for each subject from the mean time-series.

The time-series for each subjects were then divided into multiple sliding windows of varying strides $(1, 5, 10, 15)$. The window size were kept fixed at 50s following the recommendations from [58]. Absolute Pearson's correlation were calculated for each subject and each time window between the 85 regions. Note that the correlation coefficient values are bidirectional. Hence only one set of values for each pair of regions were kept and thus we get $\binom{85}{2} = 3570$ edge correlation values (or vector of size 3570×1) for each window. Correlation vectors extracted from different time-windows were stacked to form a *dynamic* functional connectivity matrix (size $3570 \times T$ where T depends on the sliding window stride). *Dynamic* functional connectivity matrix were then concatenated to form a 3 dimensional tensor of size $3570 \times T \times 475$. A workflow diagram for the proposed prediction scheme is given in Fig. 2.

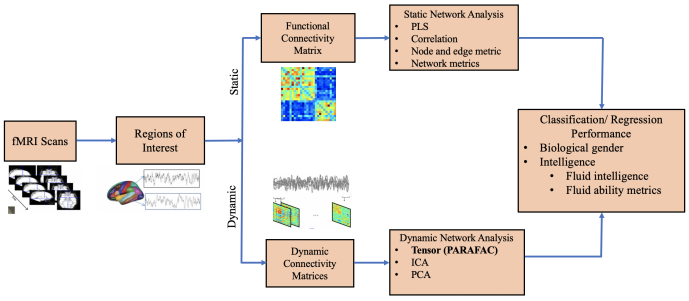

Fig. 2: The workflow for proposed classification/ regression framework. *Static* and *dynamic* connectivity matrices are extracted from brain regions. The features extracted from these matrices are used to predict biological gender and intelligence.

C. Performance Comparison

We compare the performance of proposed dFC against the following baseline methods:

Partial Least Squares (PLS) [31]: Partial least squares method is useful for associating neuroimaging markers with behavior. PLS finds a new projection of the response variables and independent variables into a new common space. PLS was run on the *static* correlation matrix extracted for the group of subjects for classification and prediction. The number of components for PLS were chosen based on cross-validation performance.

Correlation Coefficients [59]: Raw values of correlation coefficients were used as features for classification and prediction scheme. However, the number of features is very large compared to number of samples (475) and hence there is a chance of reduced prediction power for curse of dimensionality. As a result, feature selection becomes important for prediction task [22], [60]. Feature selection was implemented using Minimum Redundancy Maximum Relevance (mRMR) [61]. Note that other techniques such as Minimum Uncertainty and Sample Elimination (MUSE) [60] can select important features from larger datasets.

Network Features [62]: Adjacency matrices were used to calculate network characteristics using *Brain Connectivity Toolbox* (BCT) [3] as described in [26]. At a local (node) level in the network, three features, namely *local efficiency (LE), clustering coefficient (CC)* and *betweenness centrality (BC)*, were computed [63], [64]. At a global level, we calculated two features: *modularity* and *global efficiency* [64]. The local and global features in the network represent complementary viewpoints of the network for *segregation* and *integration* of nodes, respectively. Hence from each subject, we extracted $85 \times 3 \times 2$ (for 3 features at each node) $+ 2 \times 2$ (for *modularity and global efficiency*) $= 514$ network features.

An overview of the network based features is discussed next as described in [65]. *Local efficiency* is computed using the summation of inverse of the shortest paths to the neighbors of a node. This metric is used to understand how efficient a node is for transferring information between two neighboring nodes. *Clustering coefficient* is calculated by the number of triangles created around a node out of all possible triangles. *Betweenness centrality* of a node is calculated as the percentage of shortest paths that contain the node. *Modularity* metric measures how a network is sub-divided into smaller dense sub-networks with sparse inter-connections. *Global efficiency* describes the efficiency of information transfer within the whole graph. More details of the network measures can be found in [62].

Sub-Graph Entropy [55]: We have recently shown that sub-graph entropy metrics are well suited for identifying brain states [55] and classifying patients suffering from metal disorders [26]. From *static* one-shot connectivity matrix, node entropy and edge entropy were calculated and they were used for further analysis.

Principal Component Analysis (PCA) [48]: Principal Component Analysis was carried out on the concatenated correlation values from sliding window for all subjects. This procedure extracted common network space and unique time-

[1] https://db.humanconnectome.org
[2] https://www.humanconnectome.org/
[3] https://sites.google.com/site/bctnet/

courses for each subject that are orthonormal to each other. The average value of unique time-courses were used as features for prediction. The number of components for PCA were chosen based on cross-validation performance.

Independent Component Analysis (ICA) [19]: Independent Component Analysis is a popular method for analysis dFC. In our experiments, ICA was also carried out on the concatenated correlation values from sliding window for all subjects. Like PCA, this analysis extracted common network space and unique time-courses for each subject that are independent of each other in statistical sense. The average value of unique time-courses were used as features for prediction. The number of components for ICA were chosen based on cross-validation performance.

Mean dFC: For comparison to existing sliding window approach, average absolute Pearson correlation value for all the sliding window correlation matrices were calculated for each subject. These average edge weights of size 3570×1 are then used directly for classification (respectively, regression).

D. Statistical Analysis

We divided the dataset randomly into 5 unique sets that were later used for 5-fold cross-validation. For each of the tasks, 5-fold cross validation (CV) [66] was performed over the dataset, where 4 folds are used for training each time and the rest for testing with hyper-parameters chosen using in-fold validation. In this paper, we reported the CV accuracy as well as other performance measures such as sensitivity and specificity. For intelligence prediction, we reported normalized mean square error (MSE) as well as mean absolute error (MAE) and standard deviation of error (SD). Normalized mean square error was calculated by dividing the mean square error by the square of actual values. For all the prediction performance random forest classifier (respectively, regressor) was employed. For hyperparamter tuning, $\{2^i | i = 1, .., 7\}$ trees were trained using in-fold cross-validation. We used the inbuilt implementation of random forest (TreeBagger) available in MATLAB [4].

Additionally, t-tests were carried out to find out the connectivity maps that have statistically different loading in male *vs.* female. Similarly, Pearson's correlation test was performed to extract the connectivity components with statistically *higher* correlation values with fluid intelligence and fluid ability metrics. Note that, in both cases, the subject-wise loadings (columns of C) of the components were used for finding the statistical significance. As the test involves multiple comparisons for multiple components, the significance level (α) for rejecting the *null* hypothesis that there was no significant difference (classification task/ biological gender identification) or there was no significant correlation (regression/IQ prediction task) was fixed at 0.05 with Bonferroni correction.

IV. Results

A. Classification Results

The results for classifying biological gender and prediction of IQ are described next.

[4] www.mathworks.com

All features were able to classify gender with high accuracy. The results for using six distinct methods as described above are shown in Fig. 3. We note that the proposed dFC (tensor) turns out to be one of the two best performing features (other one is edge entropy). For individual performances in each task, features extracted from *emotion* task had the best performance for classifying male *vs.* female with accuracy, sensitivity and specificity of 0.84, 0.89 and 0.81, respectively. This was closely followed by rs-fMRI. The results of the performance for each type of features are shown in Table. II.

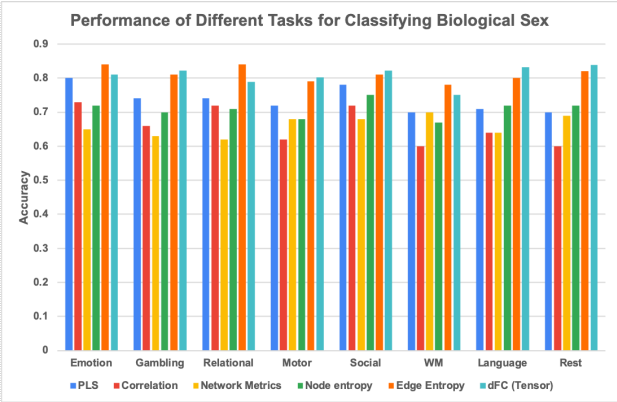

Fig. 3: Average 5-fold cross-validation accuracy for each task employing different feature engineering techniques. Here more the height of the bar, better the performance. The performance accuracy for different features in Table II are shown for each task. Our proposed dFC (Tensor) always performs within top two methods for predicting biological gender.

Overall, dFC extracted from the concatenation of tasks together performed the best in classifying biological gender. In order to understand which *stride* for calculating dFC performs the best for classifying gender, we tested the classification scheme for *stride* $= 1, 5, 10, 15$. The winning *stride* is chosen for the *"final"* classifier. The results are shown in Fig. 4. In particular, *stride* $= 10$ had best overall performance for each task where it classified biological gender most precisely for 7 out of 8 tasks.

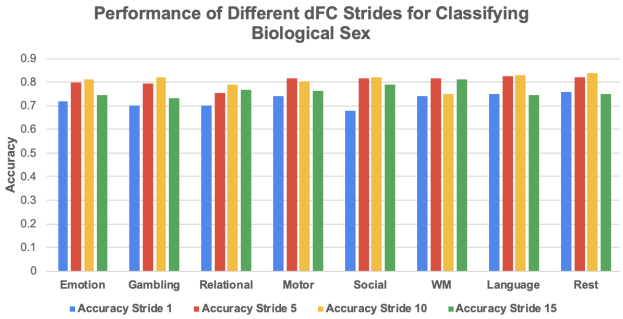

Fig. 4: Average 5-fold cross-validation accuracy for each task employing different sliding window strides for calculating dFC. Here more the height of the bar, better the performance. Stride 10 yields best accuracy most of the times.

Finally, the best performance for each class of features is shown in Table II.

TABLE II: 5-Fold cross validation classification results for biological gender classification

	Task	Features	Accuracy	Sensitivity	Specificity
Partial Least Square [31]	Emotion	15	0.80	0.66	0.86
Correlation [59]	Emotion	15	0.73	0.64	0.75
Network Features [62]	Rest	54	0.69	0.74	0.65
Node Entropy [55]	Social	85	0.75	0.83	0.66
Edge Entropy [55]	Emotion	3570	0.84	0.89	0.81
Dynamic Connectivity (Proposed)	Combined	25	**0.94**	**0.97**	**0.87**

The proposed method for classifying biological gender was compared with other ways of calculating dFC and the results are shown in Table III.

TABLE III: 5-Fold cross validation classification results for biological gender classification using different decomposition techniques from dFC.

	Task	Features	Accuracy	Sensitivity	Specificity
Tensor (Proposed)	Combined	25	**0.94**	**0.97**	**0.87**
ICA [14]	Combined	75	0.71	0.55	0.85
PCA [48]	Combined	75	0.5	0.48	0.51
Mean dFC	Emotion	3570	0.74	0.85	0.66

Fluid intelligence and Fluid ability metrics were predicted in the same way. Figs. 5 and S1 (Supplementary Information) demonstrate the results of using *static* and *dynamic* network based features for predicting fluid intelligence and fluid ability metrics, respectively. For fluid intelligence, the mean absolute error were in the range of $5-6$ for all the methods. Note that, among the tasks, working memory task was most predictive of fluid intelligence as it gave the task wise best performance for 2 out of 5 *static* connectivity features as shown in Table IV followed by emotion task. However, combining the tasks together and applying the proposed tensor decomposition yielded the best prediction performance with MSE, MAE of 0.13 and 5.1, respectively.

For fluid ability metrics, the mean absolute error were in the range of $13-16$ for all the methods. No task had a consistently good performance across all *static* connectivity features as shown in Table IV. Combining the tasks together and applying the proposed tensor decomposition yielded the best prediction performance with MSE, MAE of 0.031 and 15.37, respectively.

Additionally, Figs. 6 and S2 (Supplementary Information) show the prediction results for dFC with different sliding window strides. For fluid intelligence prediction, stride = 5 performed the best whereas for fluid ability metrics stride = 10 had the best performance.

Similar to the case of gender prediction, the winning model from each types of features and task is listed in Table IV.

The proposed method was also compared with other ways of calculating dFC (PCA, ICA) and the results are shown in Table V. The dFC based features were able to predict 27% of the variations for fluid intelligence and 22% of variations for fluid ability metrics. Both of these values are higher than that reported in [36].

To check the robustness of our results from dFC, we carried out the classification scheme using a different brain atlas based on functional organization [67]. The results on gender classification, and intelligence predictions are reported in Tables S1 and S2 (Supplementary Information). The results are always within $\sim 2\%$ of the performances compared to the anatomical brain parcellations.

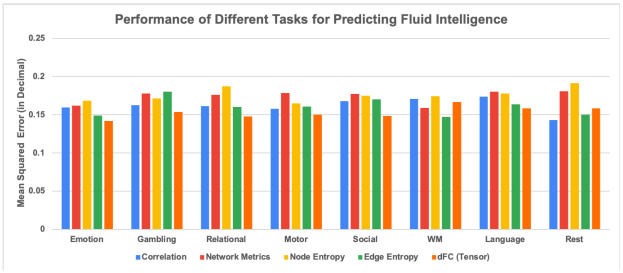

Fig. 5: Average 5-fold cross-validation normalized mean square error for each task employing different feature engineering techniques to predict fluid intelligence. The normalized mean square error performance for different features in Table IV are shown for each task. Here less the height of the bar, better the performance. Our proposed dFC (Tensor) always performs within top two methods for predicting intelligence.

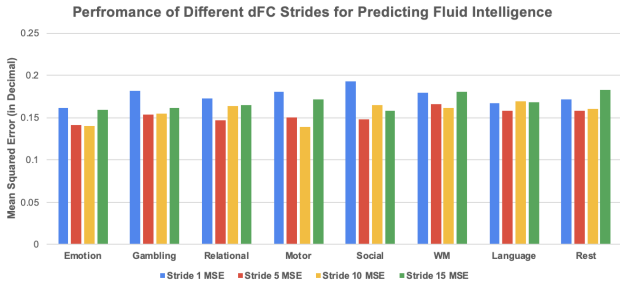

Fig. 6: Average 5-fold cross-validation normalized mean square error to predict fluid intelligence for each task employing different sliding window strides for calculating dFC. Here less the height of the bar, better the performance. Stride 5 yields best accuracy most of the times.

B. Important Networks

The dFC component maps extracted by combining sliding window correlation values across tasks were highly predictive of biological gender, and individual intelligence metrics. In order to understand if the extracted maps were loaded in significantly different ways in male *vs.* female groups, we performed t-test on the individual weight matrix (C) of the decomposed tensor. Note that columns of C correspond to loading of spatio-temporal components and the rows of C represent individual variations of different components. Hence t-tests were carried out separately on each column of C based on biological gender labels. Two components were found to be statistically different ($p < 0.002$) after Bonferroni correction of significance level. In order to visualize the component, the edges with values in the top 5% are visualized by overlaying them on an MNI brain using BrainNet toolbox [68]. The components are illustrated in Fig. 7. We see that the corresponding weights are well distributed among the subjects, which signifies that this component was prevalent in most people in the group. In particular, Spatial Map 1 in Fig. 7 has higher weights for females compared with males. On the other hand, Spatial Map 2 in Fig. 7 has higher weights for males compared with females.

TABLE IV: 5-Fold cross validation regression results for predicting IQ.

	Fluid Intelligence					Fluid Ability Metrics				
	Task	Features	MSE	MAE	SD	Task	Features	MSE	MAE	SD
Partial Least Square [31]	Emotion	15	0.58	11.42	2	Language	15	0.70	82.71	4.57
Correlation [59]	Motor	15	0.15	5.36	4.3	Relational	15	0.044	16.78	0.86
Network Features [62]	WM	425	0.15	5.35	0.33	Rest	425	0.045	17.03	3.43
Node Entropy [55]	Emotion	85	0.16	5.62	0.36	Emotion	85	0.037	15.85	1.05
Edge Entropy [55]	WM	3570	0.147	5.17	0.36	Motor	3570	0.041	15.38	0.64
Dynamic Connectivity (Proposed)	Combined	25	**0.139**	**5.1**	0.2	Combined	25	**0.031**	**15.37**	1.01

TABLE V: 5-Fold cross validation regression results for predicting IQ using different decomposition techniques from dFC.

	Fluid Intelligence					Fluid Ability Metrics				
	Task	Features	MSE	MAE	SD	Task	Features	MSE	MAE	SD
Tensor (Proposed)	Combined	25	**0.139**	**5.1**	0.2	Combined	25	**0.031**	**15.37**	1.01
ICA [19]	Combined	75	0.453	10.31	3	Combined	75	0.043	18.01	2
PCA [48]	Combined	75	0.516	11.34	4.2	Combined	75	0.087	31.49	5
Mean dFC	Motor	3570	0.169	5.80	0.13	Relational	3570	0.034	15.67	1.43

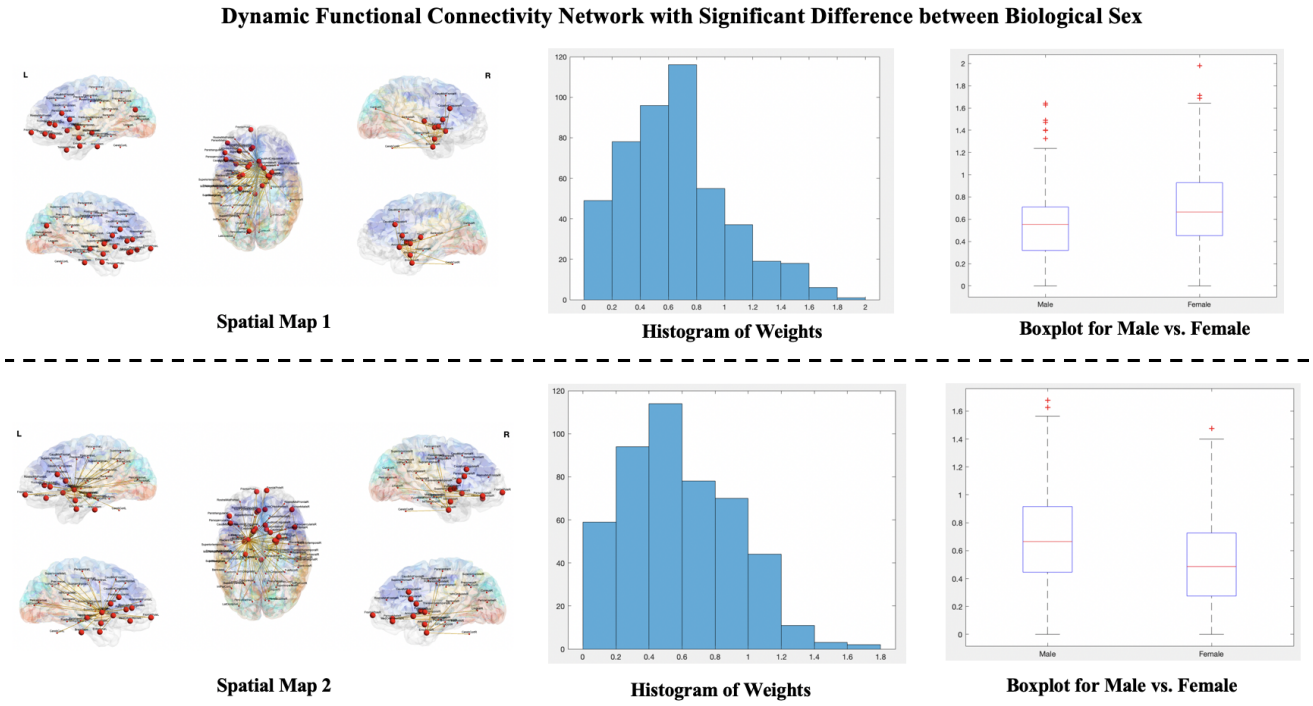

Fig. 7: Statistically significant spatial components along with the weight distributions for differentiating male *vs.* female. *Left*: Spatial map with top 5% connectivity values. *Middle*: histogram of the weight loading for all subjects. Most of the subjects have non-zero values for weights signifying that this map is present in the majority. *Right*: box-plot of the individual weights values for different biological gender groups.

To infer about the important states in the case of intelligence metrics, Pearson's correlation test is carried out on the column of C corresponding to each spatio-temporal map. In each case, there were multiple components that had $p < 0.05$, however the number of components that passed Bonferroni correction were 3 and 2 for fluid intelligence and fluid ability metrics, respectively. In both cases, two components with lowest p-values are shown in Fig. 8 and S3 in Supplementary Information, respectively. In order to visualize the component, the edges with values in the top 5% are visualized by overlaying them on an MNI brain using BrainNet toolbox [68]. For fluid intelligence, we see that the corresponding weights are well distributed among the subjects, which signifies that this component was prevalent in most people in the group. In particular, Spatial Map 1 and Spatial Map 2 in Fig. 8 have $p = 0.0012$ and $p = 0.0063$, respectively, with the fluid intelligence metric. However, for fluid ability, the corresponding weights have longer tail towards the lower range values and hence are not well distributed among the subjects. In particular, Spatial Map 1 has a negative correlation with $p = 0.0003$ and Spatial Map 2 has a positive correlation with $p = 0.0006$ with the fluid ability metric.

V. Discussion

In this paper, we presented a novel method for extracting *dynamic* functional connectivity using constrained-PARAFAC decomposition technique. Conditions for uniqueness were derived and an algorithm utilizing alternating least squares was provided to find out the unique spatio-temporal decomposition. Tensor based dFC approach was able to predict biological gender with high accuracy and intelligence with low prediction

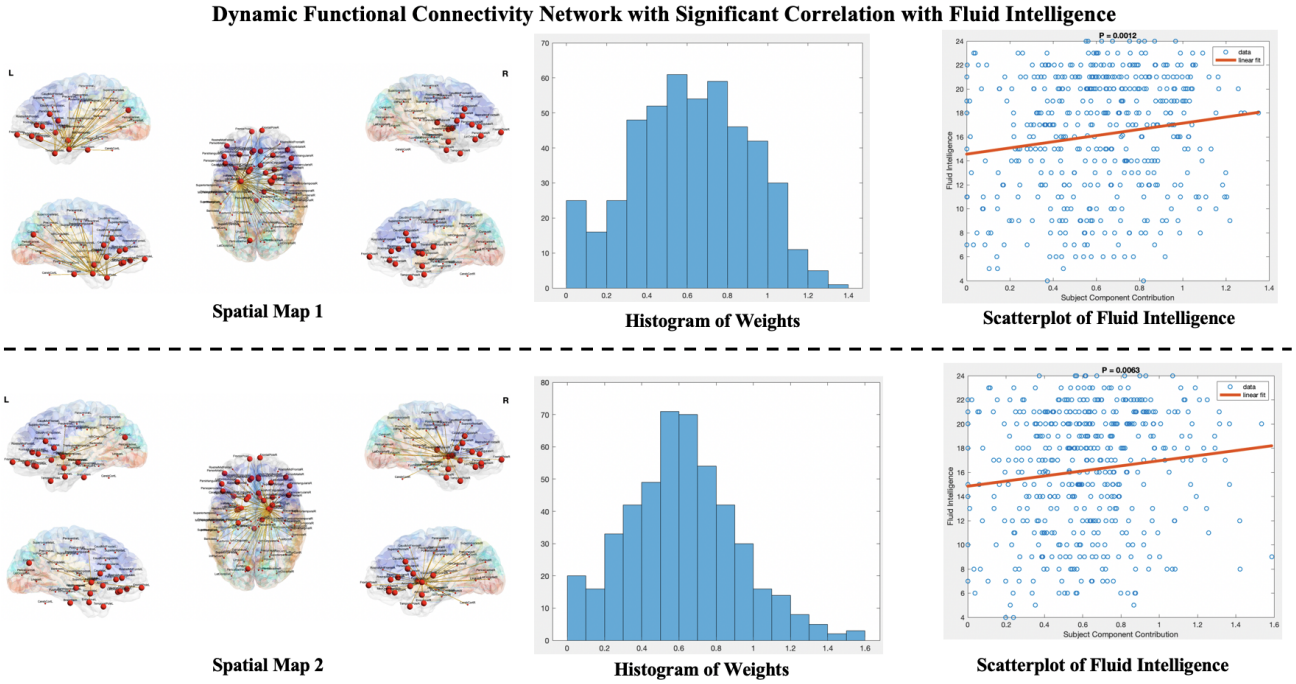

Fig. 8: Statistically significant spatial components along with the weight distributions for correlating with fluid intelligence. *Left*: Spatial map with top 5% connectivity values, *Middle*: histogram of the weight loading for all subjects. Most of the subjects have non-zero values for weights signifying that this network is present in the majority. *Right*: scatter plot with correlation curve and corresponding p-values for individual weights.

error compared with traditional *static* and *dynamic* functional connectivity based features. We also extracted the *dynamic* network maps that are associated with gender and IQ through tensor decomposition. Key observations of biological significance relative to the existing literature are described next.

A. Gender Effect on dFC

Although, biological gender has a large impact in *static* and *dynamic* brain connectivity, there are differences in scientific conclusions regarding their effects. Several connectivity studies have reported the apparent connectivity differences. The spatial map (spatial map 1) extracted from our analysis implicated regions from prefrontal cortex, precuneus and posterior cingulate cortex (PCC) that had higher connectivity in females which are similar to that reported in the previous study in [32]. Previously, in the graph theory based analysis in [59], males showed significantly higher network connections in the right hemisphere compared to females and lower left hemispheric connections compared to female group. Spatial map 1 seems to also suggest that female brain has higher functional connections to the regions in the left hemisphere. However, the connections are mainly inter-hemispherical, *i.e.,* the connections criss-cross across the central gyrus. This is also supported from anatomical connectivity literature [34]. Number of left brain regions with high functional connections is more for females compared with male. But they are mainly connected to regions in the other hemisphere. Here the component had significantly higher prevalence in females compared with males. In our work, within hemisphere connectivity is noted in spatial map 2. Here the component had significantly higher prevalence in males compared with females.

The study performed by [33] carried out statistical comparison of *static* network connectivity metrics between biological gender groups using ICA. The spatial maps found in sensorimotor, salience, attention and auditory regions showed statistically significant changes in network measures. Spatial map 2 in our analysis has a hub region in temporal lobe in the left hemisphere. The associated functional connectivity may indicate more involvement of auditory networks in most behavioral tasks for males. For Spatial map 1, well-connected regions involve pre-central and post-central regions in left hemisphere which is part of sensorimotor network whereas for spatial map 2, the regions are sparsely connected. Thus sensorimotor networks have higher inter-hemispherical connections in female whereas they have somewhat reduced inter- and intra-hemisphereical connections in males. Moreover, in our results, the predictive sub-network contains regions from salience network (hippocampus) and regions from striatum. It also contains the hippocampus which is part of salience network [26].

Dynamic functional connectivity has been shown to predict biological gender accurately in [17] (accuracy 0.80). Our proposed method employed a constrained-tensor decomposition process to extract subject dependent features which improved leave-one-out accuracy to 0.94 using dFC. Consistent with Menon et al. [17] we note that both spatial maps that had significant statistical differences involved regions from fronto-parietal and attention network (precuneus). Similarly, the spatial maps contained lateral occipital node that is part of visual network [18] in the brain. Despite these findings, more experiments need to be performed for better understanding of biological gender effect on dFC.

B. IQ Effect on dFC

There has been progress in our understanding of intelligence and its associated neural correlates using newer MRI techniques. Recent works have reported the relation between an individual's intelligence metrics and thickness in gray matter [69], white matter [70], and cortical thickness [71]. Our method extracted regions from distributed regions in brain that are correlated with intelligence metrics as shown in Figs. 8 and S3 in Supplementary Information. This was also supported in previous works on functional connectivity (FC) [72], [73]. In addition, the connectivity maps with most functional edges for fluid intelligence belong to the frontal-parietal circuit and default mode networks in the brain that was also supported in [24], [74]. Moreover, In our results, the predictive sub-network contains regions from salience network (hippocampus) and regions from striatum. Interestingly, the two significant spatial maps for fluid intelligence contain regions from different hemispheres separately (and for both cases the correlation is positive), which reinforces that fluid intelligence is a product of distributed intra-hemispheric communication. A thorough investigation using network neuroscience has confirmed that general intelligence can be associated with small world characteristics of the brain that has the potential to assert more cognitive flexibility [75] in addition to the adaptability to the information processing. However, for fluid ability metrics, spatial map 1 consisted of fronto-parietal functional networks in the left hemisphere that has negative correlation with the score. The inter-hemispheric functional connectivity for spatial map 2 in Fig. S3 in Supplementary Information may indicate that the increase in inter-hemispheric functional edges improve the fluid ability metrics.

VI. Conclusion and Future Work

This paper has demonstrated that dFC of the human brain can contribute substantially towards forming a fingerprint of biological gender and intelligence. In addition, we proposed a fully cross-validated scheme for the individual characteristic prediction. The statistically different sub-network of interest between two groups is extracted and their connection to the existing literature is drawn. Moreover, significant networks are extracted that have significantly high correlation with intelligence metrics. Future work will be directed to the lesson learned from this work to develop and plan group-specific (based on gender, IQ etc.) therapies for patients suffering from psychiatric disorders. Additionally, we will investigate the constrained tensor decompositions of *dynamic* functional connectivity for rs-fMRI where strict trilinearity is not required using PARAFAC2 decomposition. Accurately inferred spatio-temporal signal and connectivity maps from different groups can also be used to compare differences among other types of sub-groups in the population, *e.g.,* age groups, language groups, and other types of behavioral tasks.

References

[1] D. Van Essen et al., "The WU-Minn human connectome project: an overview," *NeuroImage*, vol. 80, pp. 62–79, 2013.

[2] M. Preti et al., "The dynamic functional connectome: state-of-the-art and perspectives," *NeuroImage*, vol. 160, pp. 41–54, 2017.

[3] V. D. Calhoun et al., "The chronnectome: time-varying connectivity networks as the next frontier in fMRI data discovery," *Neuron*, vol. 84, no. 2, pp. 262–274, 2014.

[4] E. Allen et al., "EEG signatures of dynamic functional network connectivity states," *Brain Topography*, vol. 31, no. 1, pp. 101–116, 2018.

[5] Y. Yang et al., "A state-space model of cross-region dynamic connectivity in MEG/EEG," in *Advances in Neural Information Processing Systems*, 2016, pp. 1234–1242.

[6] T. Roh et al., "A wearable neuro-feedback system with EEG-based mental status monitoring and transcranial electrical stimulation," *IEEE Transactions on Biomedical Circuits and Systems*, vol. 8, no. 6, pp. 755–764, 2014.

[7] Z. Zhang and K. Parhi, "Low-complexity seizure prediction from iEEG/sEEG using spectral power and ratios of spectral power," *IEEE Transactions on Biomedical Circuits and Systems*, vol. 10, no. 3, pp. 693–706, 2015.

[8] E. Al-sharoa et al., "Tensor based temporal and multilayer community detection for studying brain dynamics during resting state fMRI," *IEEE Transactions on Biomedical Engineering*, vol. 66, no. 3, pp. 695–709, 2018.

[9] C. Chang and G. H. Glover, "Time–frequency dynamics of resting-state brain connectivity measured with fMRI," *NeuroImage*, vol. 50, no. 1, pp. 81–98, 2010.

[10] R. Hutchison and J. Morton, "Tracking the brain's functional coupling dynamics over development," *Journal of Neuroscience*, vol. 35, no. 17, pp. 6849–6859, 2015.

[11] M. Yaesoubi et al., "Dynamic coherence analysis of resting fMRI data to jointly capture state-based phase, frequency, and time-domain information," *NeuroImage*, vol. 120, pp. 133–142, 2015.

[12] K. Hilger, M. Fukushima, et al., "Temporal stability of functional brain modules associated with human intelligence," *Human brain mapping*, vol. 41, no. 2, pp. 362–372, 2020.

[13] T. Chen et al., "Distinct global brain dynamics and spatiotemporal organization of the salience network," *PLoS Biology*, vol. 14, no. 6, 2016.

[14] Y. Du et al., "Interaction among subsystems within default mode network diminished in schizophrenia patients: a dynamic connectivity approach," *Schizophrenia Research*, vol. 170, no. 1, pp. 55–65, 2016.

[15] J. Su et al., "Heredity characteristics of schizophrenia shown by dynamic functional connectivity analysis of resting-state functional MRI scans of unaffected siblings," *Neuroreport*, vol. 27, no. 11, pp. 843–848, 2016.

[16] E. Damaraju et al., "Dynamic functional connectivity analysis reveals transient states of dysconnectivity in schizophrenia," *NeuroImage: Clinical*, vol. 5, pp. 298–308, 2014.

[17] S. Menon and K. Krishnamurthy, "A comparison of static and dynamic functional connectivities for identifying subjects and biological sex using intrinsic individual brain connectivity," *Scientific Reports*, vol. 9, no. 1, pp. 1–11, 2019.

[18] B. Cai et al., "A GICA-TVGL framework to study sex differences in resting state fMRI dynamic connectivity," *Journal of Neuroscience Methods*, vol. 332, pp. 108531, 2020.

[19] Y. Du et al., "Dynamic functional connectivity impairments in early schizophrenia and clinical high-risk for psychosis," *NeuroImage*, vol. 180, pp. 632–645, 2018.

[20] A. Fong et al., "Dynamic functional connectivity during task performance and rest predicts individual differences in attention across studies," *NeuroImage*, vol. 188, pp. 14–25, 2019.

[21] B. Sen and K. K. Parhi, "Extraction of common task signals and spatial maps from group fMRI using a parafac-based tensor decomposition technique," in *2017 IEEE International Conference on Acoustics, Speech and Signal Processing (ICASSP)*. IEEE, 2017, pp. 1113–1117.

[22] B. Sen and K. Parhi, "Predicting male vs. female from task-fMRI brain connectivity," in *2019 41st Annual International Conference of the IEEE Engineering in Medicine and Biology Society (EMBC)*. IEEE, 2019, pp. 4089–4092.

[23] A. Greene et al., "Task-induced brain state manipulation improves prediction of individual traits," *Nature Communications*, vol. 9, no. 1, pp. 1–13, 2018.

[24] L. Hearne et al., "Functional brain networks related to individual differences in human intelligence at rest," *Scientific Reports*, vol. 6, pp. 32328, 2016.

[25] M. D. Greicius et al., "Functional connectivity in the resting brain: a network analysis of the default mode hypothesis," *Proceedings of the National Academy of Sciences*, vol. 100, no. 1, pp. 253–258, 2003.

[26] B. Sen et al., "Sub-graph entropy based network approaches for classifying adolescent obsessive-compulsive disorder from resting-state functional MRI," *NeuroImage: Clinical*, p. 102208, 2020.

[27] L. Yao et al., "Resting tremor detection in parkinson's disease with machine learning and kalman filtering," in *2018 IEEE Biomedical Circuits and Systems Conference (BioCAS)*, 2018, pp. 1–4.

[28] D. I. Miller and D. F. Halpern, "The new science of cognitive sex differences," *Trends in Cognitive Sciences*, vol. 18, no. 1, pp. 37–45, 2014.

[29] J. M. Duarte-Carvajalino et al., "Hierarchical topological network analysis of anatomical human brain connectivity and differences related to sex and kinship," *NeuroImage*, vol. 59, no. 4, pp. 3784–3804, 2012.

[30] C. Zhang et al., "Functional connectivity predicts gender: evidence for gender differences in resting brain connectivity," *Human Brain Mapping*, vol. 39, no. 4, pp. 1765–1776, 2018.

[31] J. Zhang et al., "Gender differences in global functional connectivity during facial emotion processing: A visual MMN study," *Frontiers in Behavioral Neuroscience*, vol. 12, Article 220, 2018.

[32] R. Bluhm et al., "Default mode network connectivity: effects of age, sex, and analytic approach," *Neuroreport*, vol. 19, no. 8, pp. 887–891, 2008.

[33] E. Allen et al., "A baseline for the multivariate comparison of resting-state networks," *Frontiers in Systems Neuroscience*, vol. 5, pp. 2, 2011.

[34] M. Ingalhalikar et al., "Sex differences in the structural connectome of the human brain," *Proceedings of the National Academy of Sciences*, vol. 111, Article 2, pp. 823–828, 2014.

[35] E. Finn et al., "Functional connectome fingerprinting: identifying individuals using patterns of brain connectivity," *Nature Neuroscience*, vol. 18, no. 11, pp. 1664, 2015.

[36] J. Dubois et al., "A distributed brain network predicts general intelligence from resting-state human neuroimaging data," *Philosophical Transactions of the Royal Society B: Biological Sciences*, vol. 373, no. 1756, pp. 20170284, 2018.

[37] C. Sripada et al., "Toward a "treadmill test" for cognition: Improved prediction of general cognitive ability from the task activated brain," *BioRxiv*, p. 412056, 2018.

[38] V. Calhoun et al., "A method for making group inferences from functional MRI data using independent component analysis," *Human Brain Mapping*, vol. 14, no. 3, pp. 140–151, 2001.

[39] C. Beckmann and S. Smith, "Probabilistic independent component analysis for functional magnetic resonance imaging," *IEEE Transactions on Medical Imaging*, vol. 23, no. 2, pp. 137–152, 2004.

[40] V. Kiviniemi et al., "A sliding time-window ica reveals spatial variability of the default mode network in time," *Brain Connectivity*, vol. 1, no. 4, pp. 339–347, 2011.

[41] S. Ma et al., "Automatic identification of functional clusters in fMRI data using spatial dependence," *IEEE Transactions on Biomedical Engineering*, vol. 58, no. 12, pp. 3406–3417, 2011.

[42] M. Jafri et al., "A method for functional network connectivity among spatially independent resting-state components in schizophrenia," *NeuroImage*, vol. 39, no. 4, pp. 1666–1681, 2008.

[43] B. Cai et al., "Capturing dynamic connectivity from resting state fMRI using time-varying graphical lasso," *IEEE Transactions on Biomedical Engineering*, vol. 66, no. 7, pp. 1852–1862, 2018.

[44] E. Allen et al., "Tracking whole-brain connectivity dynamics in the resting state," *Cerebral Cortex*, vol. 24, no. 3, pp. 663–676, 2014.

[45] N. D. Sidiropoulos et al., "Tensor decomposition for signal processing and machine learning," *IEEE Transactions on Signal Processing*, vol. 65, no. 13, pp. 3551–3582.

[46] R. Bro, "PARAFAC. Tutorial and applications," in *Chemometrics and Intelligent Laboratory Systems*, 1997, vol. 38(2), pp. 149–171.

[47] T. Jiang and N. D. Sidiropoulos, "Kruskal's permutation lemma and the identification of CANDECOMP/PARAFAC and bilinear models with constant modulus constraints," *IEEE Transactions on Signal Processing*, vol. 52, no. 9, pp. 2625–2636, 2004.

[48] N. Leonardi et al., "Principal components of functional connectivity: a new approach to study dynamic brain connectivity during rest," *NeuroImage*, vol. 83, pp. 937–950, 2013.

[49] P. H. Schönemann, "A generalized solution of the orthogonal procrustes problem," *Psychometrika*, vol. 31, no. 1, pp. 1–10, 1966.

[50] A. C. Aitken, "On least squares and linear combination of observations," *Proceedings of the Royal Society of Edinburgh*, vol. 55, pp. 42–48, 1936.

[51] C. Lawson and R. Hanson, *Solving least squares problems*, vol. 15, Siam, 1995.

[52] F. Mokhtari et al., "Dynamic functional magnetic resonance imaging connectivity tensor decomposition: A new approach to analyze and interpret dynamic brain connectivity," *Brain Connectivity*, vol. 9, no. 1, pp. 95–112, 2019.

[53] D. Van Essen et al., "The human connectome project: a data acquisition perspective," *NeuroImage*, vol. 62, no. 4, pp. 2222–2231, 2012.

[54] W. Bilker et al., "Development of abbreviated nine-item forms of the ravens standard progressive matrices test," *Assessment*, vol. 19, no. 3, pp. 354–369, 2012.

[55] B. Sen et al., "Ranking regions, edges and classifying tasks in functional brain graphs by sub-graph entropy," *Scientific Reports*, vol. 9, no. 1, pp. 1–20, 2019.

[56] S. Chu et al., "Function-specific and enhanced brain structural connectivity mapping via joint modeling of diffusion and functional mri," *Scientific Reports*, vol. 8, no. 1, pp. 1–19, 2018.

[57] R. Desikan et al., "An automated labeling system for subdividing the human cerebral cortex on mri scans into gyral based regions of interest," *NeuroImage*, vol. 31, no. 3, pp. 968–980, 2006.

[58] N. Leonardi and D. Van De Ville, "On spurious and real fluctuations of dynamic functional connectivity during rest," *NeuroImage*, vol. 104, pp. 430–436, 2015.

[59] L. Tian et al., "Hemisphere-and gender-related differences in small-world brain networks: a resting-state functional MRI study," *NeuroImage*, vol. 54, no. 1, pp. 191–202, 2011.

[60] Z. Zhang and K. K. Parhi, "MUSE: Minimum uncertainty and sample elimination based binary feature selection," *IEEE Transactions on Knowledge and Data Engineering*, vol. 31, no. 9, pp. 1750–1764, 2018.

[61] H. Peng et al., "Feature selection based on mutual information criteria of max-dependency, max-relevance, and min-redundancy," *IEEE Transactions on Pattern Analysis and Machine Intelligence*, vol. 27, no. 8, pp. 1226–1238, 2005.

[62] M. Rubinov and O. Sporns, "Complex network measures of brain connectivity: uses and interpretations," *NeuroImage*, vol. 52, no. 3, pp. 1059–1069, 2010.

[63] T. Xu et al., "Network analysis of functional brain connectivity in borderline personality disorder using resting-state fMRI," *NeuroImage: Clinical*, vol. 11, pp. 302–315, 2016.

[64] B. Sen et al., "Classification of obsessive-compulsive disorder from resting-state fMRI," *IEEE 38th Annual International Conference of the Engineering in Medicine and Biology Society (EMBC)*, pp. 3606–3609, 2016.

[65] B. Sen et al., "Classification of major depressive disorder from resting-state fMRI," in *2019 41st Annual International Conference of the IEEE Engineering in Medicine and Biology Society (EMBC)*, July 2019, pp. 3511–3514.

[66] S. Arlot et al., "A survey of cross-validation procedures for model selection," *Statistics Surveys*, vol. 4, pp. 40–79, 2010.

[67] J. Power et al., "Functional network organization of the human brain," *Neuron*, vol. 72, no. 4, pp. 665–678, 2011.

[68] M. Xia et al., "BrainNet viewer: a network visualization tool for human brain connectomics," *PloS One*, vol. 8, no. 7, 2013.

[69] T. Ohtani et al., "Medial frontal white and gray matter contributions to general intelligence," *PLoS One*, vol. 9, no. 12, 2014.

[70] E. Genç et al., "Diffusion markers of dendritic density and arborization in gray matter predict differences in intelligence," *Nature Communication*, vol. 9, Article 1905, 2018.

[71] K. Narr et al., "Relationships between iq and regional cortical gray matter thickness in healthy adults," *Cerebral Cortex*, vol. 17, no. 9, pp. 2163–2171, 2007.

[72] G. Pamplona et al., "Analyzing the association between functional connectivity of the brain and intellectual performance," *Frontiers in Human Neuroscience*, vol. 9, pp. 1–11, 2015.

[73] J. Gläscher et al., "Distributed neural system for general intelligence revealed by lesion mapping," *Proceedings of the National Academy of Sciences*, vol. 107, no. 10, pp. 4705–4709, 2010.

[74] E. Santarnecchi et al., "Network connectivity correlates of variability in fluid intelligence performance," *Intelligence*, vol. 65, pp. 35–47, 2017.

[75] A. K. Barbey, "Network neuroscience theory of human intelligence," *Trends in Cognitive Sciences*, vol. 22, no. 1, pp. 8–20, 2018.

Supplementary Information: Predicting Biological Gender and Intelligence from fMRI via Dynamic Functional Connectivity

Bhaskar Sen, *Student Member, IEEE*, and Keshab K. Parhi, *Fellow, IEEE*

I. S1: Tables

TABLE S1: 5-Fold cross validation classification results for biological gender classification using different decomposition techniques from dFC (for 264 regions).

	Features	Task	Accuracy	Sensitivity	Specificity
Tensor (Proposed)	Combined	25	**0.94**	**0.96**	**0.88**
ICA	Combined	75	0.7	0.56	0.84
PCA	Combined	75	0.5	0.51	0.49

TABLE S2: 5-Fold cross validation regression results for predicting IQ using different decomposition techniques from dFC (for 264 regions).

	Fluid Intelligence					Fluid Ability Metrics				
	Task	Features	MSE	MAE	SD	Task	Features	MSE	MAE	SD
Tensor (Proposed)	Combined	25	**0.1313**	**5.05**	0.3	Combined	25	**0.0306**	**14.1**	1.21
ICA	Combined	75	0.4661	10.12	2.8	Combined	75	0.0414	17.81	2.2
PCA	Combined	75	0.5321	12.34	4.1	Combined	75	0.0866	30.79	4.97

II. S2: Illustrations

Bhaskar Sen and Keshab K. Parhi are with Department of Electrical and Computer Engineering, University of Minnesota, Minneapolis (e-mail: parhi@umn.edu)

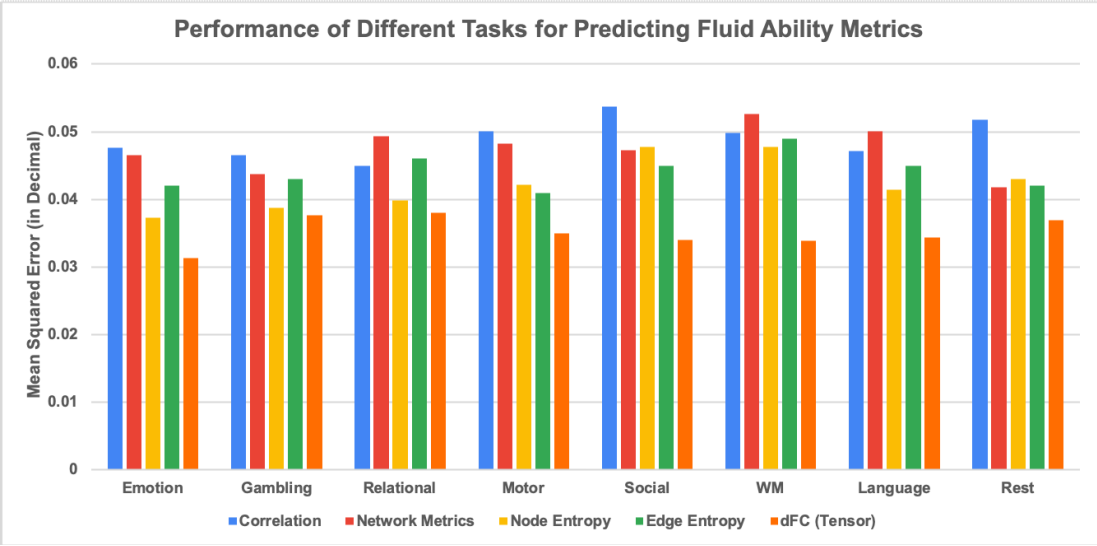

Fig. S1: Average 5-fold cross-validation normalized mean square error for each task employing different feature engineering techniques to predict fluid ability metrics. The normalized mean square error performance for different features in Table S1 are shown for each task. Here less the height of the bar, better the performance. Our proposed dFC (Tensor) always performs within top two methods for predicting biological gender.

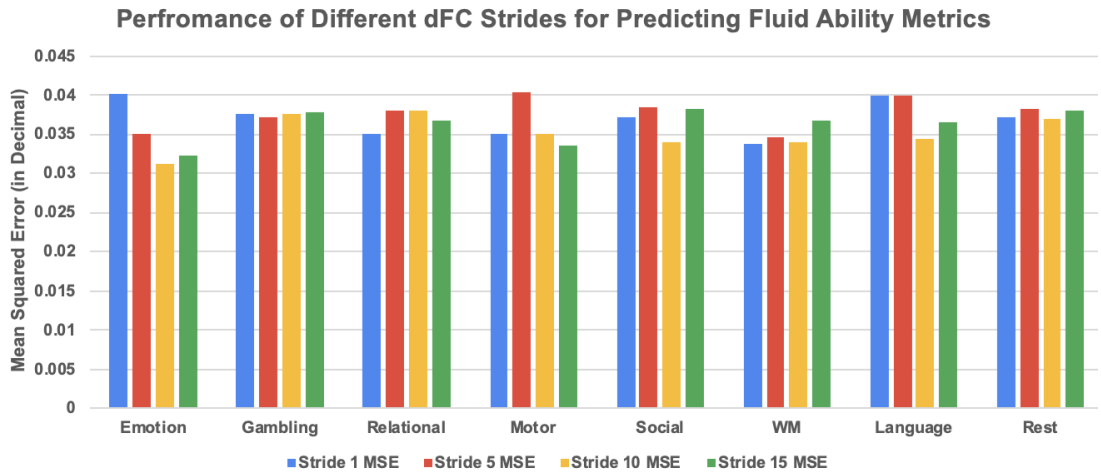

Fig. S2: Average 5-fold cross-validation normalized mean square error to predict fluid ability metrics for each task employing different sliding window strides for calculating dFC. Here less the height of the bar, better the performance. Stride 10 yields best accuracy most of the times.

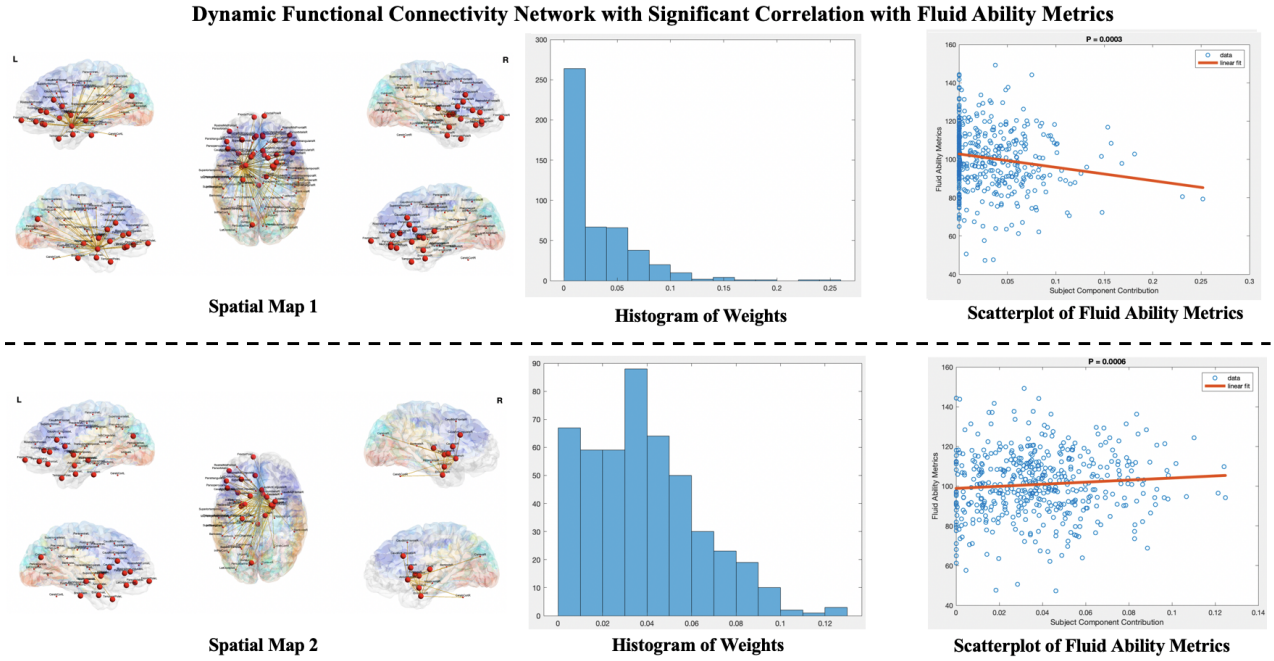

Fig. S3: Statistically significant spatial components along with the weight distributions for correlating with fluid ability metrics. *Left*: Spatial map with top 5% connectivity values. *Middle*: histogram of the weight loading for all subjects. Most of the subjects have non-zero values for weights signifying that this network is present in most of the subject. *Right*: scatter plot with correlation curve and corresponding p-values for individual weights.

S3: Atlas Details

This section provides the details of the atlas regions and their corresponding coordinates in MNI152 space.

TABLE R1: Desikan Atlas Coordinates and Regions

X	Y	Z	Region
-22.43799052	-40.01410235	-49.10043329	Left_Cerebellum_Cortex
-9.365745637	2.239886304	-14.37367795	Left_Thalamus_Proper
-10.07260101	27.72348485	-12.26073232	Left_Caudate
-21.98422754	20.16952115	-20.84432891	Left_Putamen
-16.83028771	16.79043546	-23.15999222	Left_Pallidum
-0.075123916	-9.236922464	-48.42339352	Brain_Stem
-20.50547599	-2.062973884	-30.15532856	Left_Hippocampus
-19.81226823	15.48516687	-36.92135352	Left_Amygdala
-7.276182432	31.04307432	-27.10304054	Left_Accumbens_area
21.48534428	-39.86756307	-49.02782405	Right_Cerebellum_Cortex
9.483949985	2.061275227	-13.59662913	Right_Thalamus_Proper
11.78609914	26.20757004	-11.62715517	Right_Caudate
22.79048673	20.47876106	-20.71349558	Right_Putamen
17.75835396	15.67295792	-21.86726485	Right_Pallidum
22.00855593	-1.230696995	-31.1206177	Right_Hippocampus
20.08349546	15.711738	-37.17331388	Right_Amygdala
6.856174699	29.9811747	-26.78840361	Right_Accumbens_area
-46.56135363	-24.43048423	-8.671588408	ctx_lh_bankssts
-2.641475645	34.52602674	4.327244508	ctx_lh_caudalanteriorcingulate
-29.18799213	34.20815342	18.68062611	ctx_lh_caudalmiddlefrontal
-8.394193234	-59.99674691	0.810426155	ctx_lh_cuneus
-21.87644009	14.07402074	-47.78801843	ctx_lh_entorhinal
-30.9386489	-27.44044884	-34.66050092	ctx_lh_fusiform
-38.44759259	-46.19018519	10.055	ctx_lh_inferiorparietal
-45.16522307	-13.35528397	-36.35213969	ctx_lh_inferiortemporal
-6.797138047	-26.52777778	-0.606060606	ctx_lh_isthmuscingulate
-28.81817994	-68.91491475	-14.09027893	ctx_lh_lateraloccipital
-21.51043029	49.65374052	-35.04103453	ctx_lh_lateralorbitofrontal
-12.85870064	-50.95184803	-21.89164371	ctx_lh_lingual
-5.424302789	52.46314741	-33.96962151	ctx_lh_medialorbitofrontal
-51.38255075	-1.05607361	-29.19242037	ctx_lh_middletemporal
-20.70094021	-10.09763742	-33.50470106	ctx_lh_parahippocampal
-6.551643921	-8.080024814	28.71665633	ctx_lh_paracentral
-39.82481355	38.1677284	-3.969468614	ctx_lh_parsopercularis
-37.70623742	60.72183099	-31.45120724	ctx_lh_parsorbitalis
-41.22619629	47.33825684	-19.5916748	ctx_lh_parstriangularis
-11.2699553	-63.45146871	-10.27378672	ctx_lh_pericalcarine
-37.7076791	-0.500245339	17.57396958	ctx_lh_postcentral
-4.185311284	-0.283722438	12.20330739	ctx_lh_posteriorcingulate
-35.30378452	13.60621618	15.33101499	ctx_lh_precentral
-8.750484872	-38.07336113	13.38877036	ctx_lh_precuneus
-3.369775542	54.56656347	-17.64705882	ctx_lh_rostralanteriorcingulate
-27.43047381	65.73664656	-9.245512066	ctx_lh_rostralmiddlefrontal

X	Y	Z	Region
-8.409821118	46.32435307	13.8764545	ctx_lh_superiorfrontal
-21.121497	-41.68930512	23.69906348	ctx_lh_superiorparietal
-46.72014687	8.292424968	-21.74289591	ctx_lh_superiortemporal
-46.00677227	-13.25964187	10.55130854	ctx_lh_supramarginal
-5.798690205	78.87528474	-29.70529613	ctx_lh_frontalpole
-25.94376504	31.79330393	-52.99268244	ctx_lh_temporalpole
-36.91558442	-0.342938312	-11.6599026	ctx_lh_transversetemporal
-30.75487945	20.2217279	-20.08969575	ctx_lh_insula
48.03367217	-19.09704574	-10.55749682	ctx_rh_bankssts
5.245158888	35.7336147	3.08031281	ctx_rh_caudalanteriorcingulate
31.32239106	30.37378154	20.14012328	ctx_rh_caudalmiddlefrontal
5.413062284	-61.50735294	2.649221453	ctx_rh_cuneus
19.14095007	13.38072122	-47.39684466	ctx_rh_entorhinal
30.54333274	-25.02878436	-34.88151553	ctx_rh_fusiform
40.10512232	-41.90762888	9.178134557	ctx_rh_inferiorparietal
43.5415707	-8.394461078	-39.20629894	ctx_rh_inferiortemporal
5.855446927	-27.09696728	-1.528830806	ctx_rh_isthmuscingulate
28.27539489	-65.8775836	-18.00317174	ctx_rh_lateraloccipital
21.03270609	48.73015873	-34.47388633	ctx_rh_lateralorbitofrontal
9.887762593	-49.87773888	-19.71100632	ctx_rh_lingual
4.966974573	55.82042114	-33.24071315	ctx_rh_medialorbitofrontal
50.85591502	-4.637917276	-30.79573414	ctx_rh_middletemporal
21.59495927	-9.769602851	-33.93711813	ctx_rh_parahippocampal
5.574623858	-6.455534659	29.1560317	ctx_rh_paracentral
43.43193444	33.05039788	-5.577159909	ctx_rh_parsopercularis
39.84943842	55.80170411	-30.06438807	ctx_rh_parsorbitalis
44.60538203	44.68959732	-16.17094734	ctx_rh_parstriangularis
10.07145966	-62.11767266	-9.486723738	ctx_rh_pericalcarine
37.2218269	-2.29390681	18.21908602	ctx_rh_postcentral
4.539522514	1.299480455	13.94575705	ctx_rh_posteriorcingulate
35.74047669	11.18046754	17.23375229	ctx_rh_precentral
7.952909887	-39.13619703	12.41339621	ctx_rh_precuneus
5.23004886	53.77137622	-18.7896987	ctx_rh_rostralanteriorcingulate
29.98936817	63.1596294	-6.599787363	ctx_rh_rostralmiddlefrontal
10.21130626	44.56652488	15.72779455	ctx_rh_superiorfrontal
19.52022891	-44.67677003	23.1629292	ctx_rh_superiorparietal
47.22200315	10.34015441	-23.27712519	ctx_rh_superiortemporal
46.5050845	-10.93363136	9.673192179	ctx_rh_supramarginal
7.123893805	80.40376106	-25.63053097	ctx_rh_frontalpole
22.85859073	30.3030888	-51.48117761	ctx_rh_temporalpole
38.81806931	1.170792079	-13.0730198	ctx_rh_transversetemporal
32.27828362	19.71071121	-21.13080728	ctx_rh_insula

Proofs

The optimization is stated as:

$$\min_{\tilde{\mathcal{X}}} ||\mathcal{X} - \tilde{\mathcal{X}}||_F^2 \ s.t.\ \tilde{\mathcal{X}} = (A, B, C), A^T A \ = \ I, \ C \geq 0 \tag{1}$$

A. Theorem 1.

Consider $\mathcal{X} \in \mathcal{R}^{I_1 \times I_2 \times I_3}$. Let $A \in \mathcal{R}^{I_1 \times F}, B \in \mathcal{R}^{I_2 \times F}, C \in \mathcal{R}^{I_3 \times F}$ represent the tensor decomposition matrices such that $C \geq 0$ and $A^T A = I$. In this case a global minimum for (1) exists. In other words, there is only one solution for $\tilde{X}$ that minimizes (1).

Proof. We prove this theorem following Proposition 3.1 of [1]. Note that (1) can be written in unfolded format as follows,

$$\min_{A,B,C} ||X_2 - (A \odot C)B^T||_F^2 \ \ s.t.\ A^T A \ = \ I, \ C \geq 0 \tag{2}$$

Let us denote, $f(A, B, C) = ||X_2 - (A \odot C)B^T||$. Solving (1) is equivalent to finding the minimum for $f(A, B, C)$. Since $A^T A = I$, $(A \odot C)^T (A \odot C) = I$. Thus solving for B, $B^T = [(C \odot A)^T X_2]$. Substituting B^T into (2) yields,

$$g(A, C) = ||X_2 - (A \odot C)(A \odot C)^T X_2||_F^2 \tag{3}$$

Note that $A^T A = I$ and $C \geq 0$. In addition, g is continuous and the domain of g is compact (as the domain of A, B are continuous and compact). Thus the global minimum exists for g. As a result, f has a global minimum. ■

B. Theorem 2.

If conditions *I* and *II* are satisfied, then the decomposition $\tilde{X} = (A, B, C)$ is unique up to permutation and scaling.

Proof. This can be proved by closely following the proof for the unrestricted case as given in [2]. The only difference is the relaxation of restriction on the columns of C in our case. Note that the restrictions on columns for A to be a full column rank is fully satisfied by the fact that $A^T A = I$

Let $BC = (B \odot C)$. Conditions *I* and *II* imply that the non-trivial combination of BC can not be written as represented as tensor product of two vectors which satisfies the necessary and sufficient conditions of [2]. ■

1) Algorithm for Solving the Problem: An algorithm for finding the solution of (1) is given in Algorithm S1.

Algorithm S1: Alternating Least Square Algorithm for Solving Constrained PARAFAC in (1)

Input : Tensor $\mathcal{X}$, rank F
Output: Estimated connectivity maps A, time courses B, subject-wise contribution C
(X_1, X_2, X_3) = Unfold $\mathcal{X}$ along axis 1, 2, 3 respectively.
Initialize A, B, C
for $i = 1$ **to** *until convergence* **do**
  % Solve for A from unfolding X_1
  $M = [(B \odot C)^T X_1]$
  $M = U \Sigma V^T$
  $A^T = U V^T$
  % Solve for B from unfolding X_2
  $B^T = [(C \odot A)^T X_2]$
  % Solve for C from unfolding X_3
  $N = (A \odot B)^T X_3$
  $C^T = [N_+]$ where N_+ contains only the positive elements of N
end

C. Theorem 3.

Algorithm S1 finds the uniquely identifiable decomposition of (1).

Proof. The Lagrangian for (1) can be written as

$$L(A, B, C, \Lambda_1, \Lambda_2) = ||X_2 - (A \odot C)B^T||_F^2 + Tr(\Lambda_1(A^T A - I)) + Tr(\Lambda_2(-C))$$

The domain sets of A, B and C are in $R^{I_1 \times F}, R^{I_2 \times F}$ and $R^{I_3 \times F}$, respectively, and hence they are convex sets. Note that every update in Algorithm S1 is an optimal update for each sub-problem. Using proposition 2.7.1 of [3], (A^*, B^*, C^*) is a stationary point.

For the unconstrained PARAFAC decomposition, there does not exist any proof of convergence, which may not converge, or converge to a local minimum [4]. However, there exists research that describes global convergence for block-nonlinear alternating least square under convex constraints. As the function $||X_2 - (A \odot C)B^T||_F^2$ is quasi-convex on $R^{I_1 \times F} \times R^{I_2 \times F} \times R^{I_3 \times F}$, according to Proposition 5 of [5],(A^*, B^*, C^*) is a critical point of (1). From Theorem 1, (A^*, B^*, C^*) finds the uniquely identifiable decomposition of (1). ■.

REFERENCES

[1] M. Sørensen, L. Lathauwer, et al., "Canonical polyadic decomposition with a columnwise orthonormal factor matrix," *SIAM Journal on Matrix Analysis and Applications*, vol. 33, no. 4, pp. 1190–1213, 2012.
[2] T. Jiang and N. D. Sidiropoulos, "Kruskal's permutation lemma and the identification of CANDECOMP/PARAFAC and bilinear models with constant modulus constraints," *IEEE Transactions on Signal Processing*, vol. 52, no. 9, pp. 2625–2636, 2004.
[3] D. P. Bertsekas, "Nonlinear Programming: Second Edition," *Athena Scientific*, 1999.
[4] P. Comon, X. Luciani, and A. De Almeida, "Tensor decompositions, alternating least squares and other tales," *Journal of Chemometrics: A Journal of the Chemometrics Society*, vol. 23, no. 7-8, pp. 393–405, 2009.
[5] L. Grippo and M. Sciandrone, "On the convergence of the block nonlinear Gauss–Seidel method under convex constraints," *Operations Research Letters*, vol. 26, no. 3, pp. 127–136, 2000.